Received: 12 June 2020 | Revised: 15 September 2020 | Accepted: 30 September 2020
DOI: 10.1049/elp2.12024

IET Electric Power Applications
The Institution of Engineering and Technology
WILEY

ORIGINAL RESEARCH PAPER

Comparison of rare-earth and hybrid-magnet mover configurations for a permanent magnet synchronous linear motor

Xiaomei Liu[1] | **Haitao Yu**[2] | **David Gerada**[3] | **Zeyuan Xu**[3] | **Hongbo Qiu**[1] | **Wanying Jia**[1] | **Cunxiang Yang**[1]

[1]College of Electrical and Information Engineering, Zhengzhou University of Light Industry, Zhengzhou, China

[2]College of Electrical Engineering, Southeast University, Nanjing, China

[3]Department of Electrical and Electronic Engineering, University of Nottingham, Nottingham, UK

Correspondence

Xiaomei Liu, College of Electrical and Information Engineering, Zhengzhou University of Light Industry, No. 5 Dongfeng Road, Zhengzhou, China.
Email: lxm812@outlook.com

Funding information

Key Projects of Science and Technology of Henan Province, Grant/Award Number: 202102310284

Abstract

Force ripple and cost reduction are two of the main challenges in optimising the design and increasing the market uptake of permanent magnet synchronous linear motors (PMSLM). Two mover configurations are compared in depth; one made entirely from rare-earth materials while another consisting of a hybrid (rare-earth/ferrite) magnet layout. First, the rare-earth PMSLM is optimised and designed. Based on the same design and simulation methods, a hybrid PM materials with structure PMSLM is then proposed, optimised and designed using NdFeB at the centre pole-section and ferrite at the edges. The two configurations of the PMSLM and their relative merits/demerits are compared using the simulation results of the flux density distribution in the air gap, back electromotive force (EMF), and cogging force. The hybrid-magnet structure PMLSM has a better magnetic performance, and the force ripple is reduced by around 1%. Furthermore, the magnet material cost of the hybrid-magnet PMLSM is reduced by nearly 25% compared with the original PMLSM. Finally, a prototype of the rare-earth and hybrid-magnet PMSLM is manufactured and tested to validate the modelling techniques and the results.

1 | INTRODUCTION

Permanent magnet synchronous linear motors (PMSLM) are widely used in industrial manufacture, railway transportation, etc. due to the advantages of simple structure, reliable operation, high performance and small size [1]. The cost of permanent magnet motors is still a sensitive issue and often a barrier to mass proliferation in specific markets because of the heavy use of rare-earth permanent magnet materials, such as NdFeB and SmCo [2,3]. In light of this, it is necessary to conduct research on high performance motors with a goal to decrease the usage amount of rare-earth material.

Furthermore, for the PMSLM, the reduction of the cogging force is often a critical design aspect. Thus, in the process of reducing the cost of PMSLMs, the cogging force should not be sacrificed. Many methods have been proposed in the aspect of optimising the structure of PMLM to reduce the cogging force. Apart from the universal methods, such as the careful selection of slot and pole pitch combination, skewed pole, skewed slot, and auxiliary teeth [1, 4]. Some literatures have reported that the efficiency and performance of the electrical machines will be improved with an almost sinusoidal flux density distribution in the air gap region [5–7]. Moreover, some special structures have been proposed, such as quasi-Halbach magnetization structure in Reference [3] and convex pole structure of permanent magnet in Reference [4]. While the aforesaid methods are useful in reducing the cogging force of PMSLM, the rare-earth material usage tends to increase in adopting these methods.

According to the electromagnetic performance of different PM materials, the change of PM material also affects the flux density distribution of electric machines. Ferrite is one of the allotropes iron that is stable at room temperature and pressure. Recently, the application of ferrite in different radial-motor rotor topologies including spoke type [8], multi-layer U and V shapes [9], and novel LC type [10] is becoming more and more popular to improve the force density, thus reducing the cogging force and the manufacturing cost. Indeed, the combined use of rare-earth permanent magnet materials and ferrite can change the flux density in the airgap similar to the method of changing the PM shapes.

A method of using ferrite to replace sectional areas of the NdFeB magnet is proposed and compared to an all-rare-earth solution. Although the coercivity and magnetic energy of ferrite is only 10% of the NdFeB, combined performance/cost benefits are found when they are used in combination and by appropriate design. This study is organised as follows: a rare-earth PMSLM and its analysis are described in Section II. Based on the rare-earth design and simulation method, a proposed structure PMSLM with hybrid PM materials is presented in Section III. In Section IV, the hybrid structure is described and optimised, with the relative performances analysed. Experimental model verification is conducted in Section V. The relative merits and demerits of the two mover configurations researched in this paper are finally summarised in Section VI.

2 | TOPOLOGY OF RARE-EARTH PERMANENT MAGNET SYNCHRONOUS LINEAR MOTORS AND ITS FORCE ANALYSIS

2.1 | Structure of the rare-earth permanent magnet synchronous linear motors

This section presents the rare-earth PMSLM. The basic structure parameters are shown in Table 1, and its 3D structure is shown in Figure 1, which contains a primary mover and a secondary mover. The primary is made up of silicon-iron laminations and contains nine slots and two auxiliary teeth. The secondary mover is composed of a back iron and surface-mounted PMs, the effective pole number is 10, and the material for the PMs is NdFeB. Through the optimisation of the size of magnets, teeth, and the auxiliary teeth on the end by numerical FEA, the force ripple of this PMSLM can be optimised down to 3.33%. In order to meet the magnetic and thermal performance, the mean force is 312.7 N, for a current density of 5 A/mm^2.

2.2 | Cogging force analysis of permanent magnet synchronous linear motors

To explain the proposed mover structure, which is based on the use of a variable air-gap length, the cogging force analysis is presented in this section. The thrust of the rare-earth PMSLM is determined by using the co-energy as [11]:

TABLE 1 Basic structure parameters of the original permanent magnet synchronous linear motors (PMSLM)

Parameters	Value	Parameters	Value
τ_s	20 mm	h_m	4 mm
τ_n/τ_p	0.6	h_w	100 mm
τ_p	18 mm	R_F	3.33%
g	1 mm	F_{mean}	312.7 N
d_i	5 A/mm^2	F_{cogging}	3.4 N
s	0.6	E_P	579.9 N

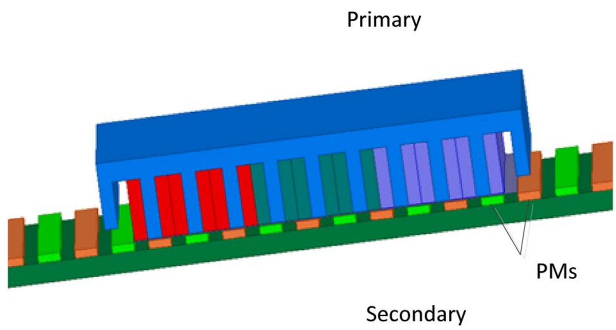

FIGURE 1 Original permanent magnet synchronous linear motors (PMSLM)

$$F = \frac{\partial W}{\partial x}\Big|_{i=\text{constant}} \tag{1}$$

Assuming that the magnetic permeability of the armature core is infinite, the magnetic field energy in airgap can be expressed as follows:

$$W \approx \frac{1}{2\mu_0}\int B^2 dV \tag{2}$$

In order to analyse the magnetic distribution in the airgap of this PMSLM, a three-region analytical model is established, as shown in Figure 2, consisting of the airgap and windings region (I), the PMs region (II), and the iron region (III). The magnetic field produced by the magnets is computed using Maxwell's equations.

The governing field equation for this magnetic field in terms of magnetic potential A_1 of region I and A_2 of region II can be described by [12,13]:

$$\begin{cases} \nabla^2\vec{A} = 0 \\ \nabla^2\vec{A} = -u_0\vec{J}_M \end{cases} \tag{3}$$

where $\vec{J}_M = \nabla\times\vec{M}$, and is given by:

$$\vec{M} = M_x a_x + M_y a_y \tag{4}$$

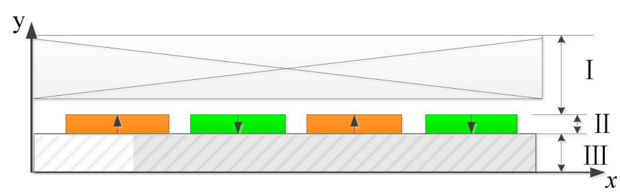

FIGURE 2 Analytical layer model of permanent magnet synchronous linear motors (PMSLM)

In the above equation M_x and M_y can be expressed as a Fourier series.

$$M_x = \sum_{n=1,3\ldots}^{\infty} P_n \sin\left(\frac{m_n \tau_p}{2}\right)\cos(m_n x)$$
$$M_y = \sum_{n=1,3\ldots}^{\infty} P_n \cos\left(\frac{m_n \tau_p}{2}\right)\sin(m_n x) \tag{5}$$

where $P_n = 4B_r/n\pi$ and $m_n = n\pi/\tau$.

The boundary conditions are:

$$\begin{aligned} &H_{2x}\big|_{y=0} - H_{1x}\big|_{y=0} = \mathrm{M}_x \\ &H_{1x}\big|_{y=-\mathrm{h_m}} = -\mathrm{M}_x \\ &H_{1x}\big|_{y=\mathrm{g}+\mathrm{h_w}/2} = 0 \\ &\mathrm{B}_{1\mathrm{y}}\big|_{y=0} = \mathrm{B}_{2\mathrm{y}}\big|_{y=0} \end{aligned} \tag{6}$$

Through calculating the Equation (1), the tangential and normal flux density of the components (B_x and B_y) produced by the PMs in the air gap (region I) are as follows:

$$B_{1x}(x,y) = \sum_{n=1,3\ldots}^{\infty} m_n\left[a_{1n}e^{m_n y} - b_{1n}e^{m_n y}\right]\cos(m_n x)$$
$$B_{1y}(x,y) = \sum_{n=1,3\ldots}^{\infty} m_n\left[a_{1n}e^{m_n y} - b_{1n}e^{m_n y}\right]\sin(m_n x) \tag{7}$$

In Equation (7), a_{1n} and b_{1n} are given by:

$$\begin{aligned} a_{1n} = &\left(\frac{P_n\mu_0}{2m_n e^{2m_n}(h_m + g + h_w) + m_n}\right)\cdot\left[\sin\left(\frac{m_n\tau_p}{2}\right)\right. \\ &+ \cos\left(\frac{m_n\tau_p}{2}\right)e^{2m_n h_m} + 2\sin\left(\frac{m_n\tau_p}{2}\right)e^{m_n h_m} \\ &\left.+ \sin\left(\frac{m_n\tau_p}{2}\right) - \cos\left(\frac{m_n\tau_p}{2}\right)\right] \\ b_{1n} = &\, e^{2m_n(g+h_w)}\cdot a_{1n} \end{aligned} \tag{8}$$

Through the above analysis, it can be seen that the thrust force of the PMSLM has a close relationship with the sinusoidal property caused by PMs.

2.3 | End effect force analysis of PMSLM

End effect force is a unique characteristic of linear motors, which is caused by the disconnection of the magnetic field in the back iron. This force is mainly affected by the length of the primary and the end structure, and the force of the two end-sides has the same amplitude but opposite direction [12,13], which is calculated by the following equation:

$$F = F_L - F_R = L_a \int\left(\frac{B_{0x1}^2(y) - B_{0x2}^2(y)}{2\mu_0}\right)dy \tag{9}$$

The end-flux density of the PMSLM can be obtained by the following equation:

$$B_{0y}(x) = B_y(x)\cdot G \tag{10}$$

where B_y(x) can be obtained from Poisson's equation, expressed as:

$$B_y(x) = \sum_{n=1}^{\infty} B_{2n-1}\cdot\cos\left[\frac{(2n-1)\pi\cdot(x-\Delta)}{\tau}\right] \tag{11}$$

There is a one-to-one correspondence between the normal flux density of the end-face and the y-component of the end flux density:

$$\begin{cases} B_{0x1}(y) = B_{0y}(-b - y - wf) \\ B_{0x2}(y) = B_{0y}(b + y + wf) \end{cases} \tag{12}$$

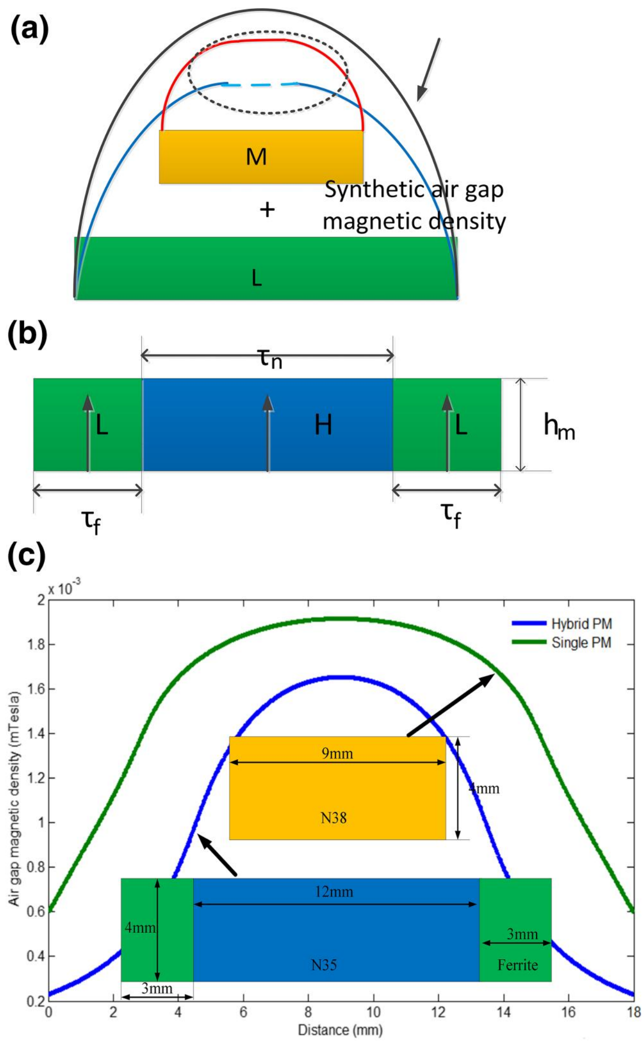

FIGURE 3 Principle and structure of the proposed PM structure. (a) Principle of the proposed PM structure, (b) the proposed PM structure, and (c) Air gap magnetic density of single PM and hybrid PM

Through substituting Equations (10)–(12) into Equation (9) and ignoring the higher-order harmonics, the expression of the end effect detent force for the primary iron becomes:

$$f_{core} = -\frac{L_a B_1^2}{2\mu_0} \int \sin \frac{2\pi (b + y + w_f)}{\tau} . G^2 dy . \sin \frac{2\pi\Delta}{\tau} \quad (13)$$

Therefore, from Equation (13), the amplitude of the fundamental component B_1 of the normal flux density of the end-face acts on the end-effect detent force. Therefore, the sinusoidal property of the end-flux density curve will also affect the amplitude of the end effect detent force, while this value is also affected by the position of the mover (i.e., affected by the displacement of the mover Δ)

3 | FORMING A MORE SINUSOIDALLY SHAPED FLUX DENSITY DISTRIBUTION

From the foregoing analysis of part B in Section II, it can be noticed that the cogging force of a PMSLM has a close relationship with the air-gap flux density, and in-turn, the flux density in airgap (region I) has a close relationship with the remanence and sizes of the PMs. As described in Reference [14], approximate sinusoidal-shape flux density distributions can be achieved by sinusoidally shaped PMs.

The flux density distribution of a conventional pole with a single PM material is inherently non-sinusoidal and has a flat region at the top of the real flux density distribution, as described by the imaginary line in Figure 3(a), which results in more harmonics in the flux density distribution and non-optimal performance of the electric machine. It follows that if there is another flux density that could 'fill' the flat wave, and make it closer to a sinusoidal wave, the performances of the PMLM such as the cogging force and back electromotive force (back EMF) will be improved [15].

Indeed it can be qualitatively understood that it is possible to obtain a sinusoidal flux density waveform by combining different PM materials together. For the hybrid structure PM section, the combination of high flux density material (NdFeB) PM and low flux density material (ferrite) PM can be applied, as shown in Figure 3(b). In this figure, the material in the middle is high flux density PM (NdFeB), while the side material is lower flux density PM (ferrite). These are arranged as shown

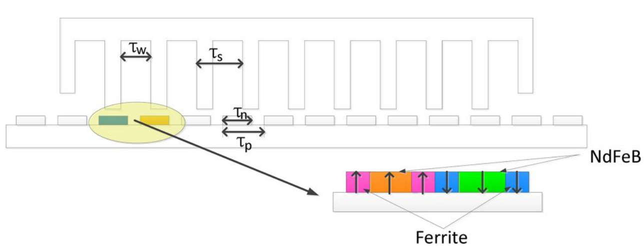

FIGURE 4 Topology of the proposed hybrid-magnet permanent magnet synchronous linear motors (PMSLM)

TABLE 2 Parameters of NdFeB and ferrite magnets

Type	Remanence (b)	Coercive force (Hc)
NdFeB(38)	≈1.24 T	≈876 kA/m
Y40(ferrite)	≈0.449 T	≈330 kA/m

TABLE 3 Analysis the ratio of NdFeB and ferrite

Ratio_n	Ratio_m	F_{mean}/N	F_{ripple} (%)	THD of voltage
0.5	0.15	308.2	2.14	1.1233
0.5	0.2	312.3	2.6	1.3557
0.5	0.25	313.893	2.42	1.1198
0.4	0.15	270.74	2.13	1.1322
0.4	0.2	279.107	2.59	1.2225
0.4	0.25	283.89	2.01	1.09822

TABLE 4 Ratio of two different PM materials in one pitch of three models

Model	Ratio_n	Ratio_m
Model 1	0.6	0
Model 2	0.5	0.25*2
Model 3	0.5	0

in Figure 3(a), and through the combination use of NdFeB and ferrite, the synthetic air gap magnetic density curve will be closer to sinusoidal. For example, the air gap magnetic density curves of the single PM (N38) and the hybrid PMs (N35 and ferrite) are shown in Figure 3(c), where the curves produced by the hybrid PMs arrangement are more sinusoidal.

For this proposed hybrid structure PMSLM, the primary is the same as with the original PMLM, while the surface-mounted PM structure is composed of two different PM materials, as shown in Figure 4. Ferrite and NdFeB are used in this PM structure of the proposed model (hereafter referred to as model 2), with ferrite PMs added to both sides of the NdFeB for each pole, with the magnetisation direction of these ferrite magnets being the same as with the middle NdFeB.

4 | SENSITIVITY ANALYSIS AND COMPARISON OF HYBRID MAGNET PERMANENT MAGNET SYNCHRONOUS LINEAR MOTORS AND RARE-EARTH MAGNET PERMANENT MAGNET SYNCHRONOUS LINEAR MOTORS

Improving the magnetic performance of the hybrid-magnet PMSLM and reducing the usage amount of NdFeB are two design objectives. The section describes the related analysis, how to arrange these two different PM materials and the impact on the mean force, as well as the force ripple.

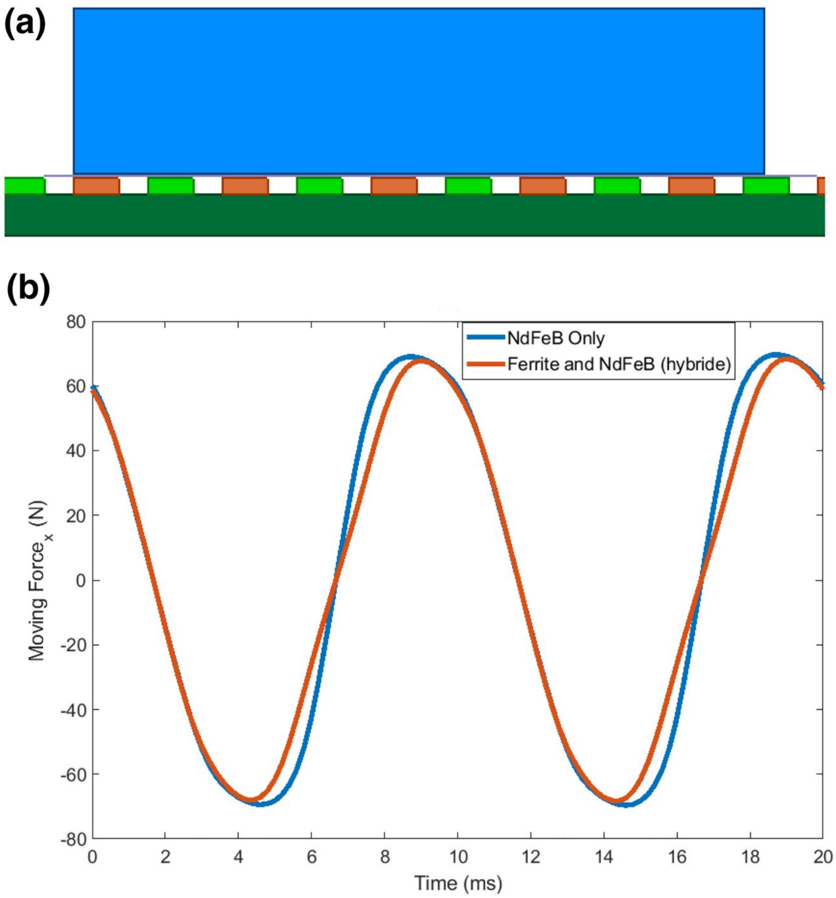

FIGURE 5 End effect force model and calculation results. (a) End effect force simulation model and (b) moving force curves of model 1 and model 2

4.1 | Improving the magnetic performance of the permanent magnet

Two objectives are sought; one is reducing the force ripple to enhance the performance, and another is reducing the amount of rare-earth PM material to reduce the material costs. The objective is done through adjusting the ratio of NdFeB and ferrite (i) to make the force ripple and harmonic of back distortion (THD) of back EMF smallest and (ii) to maintain the mean force or enhance the mean force, namely:

Minimum Force ripple (*ratio_n*, *ratio_m*), THD.

Maximum F_{mean} (*ratio_n*, *ratio_m*) where ratio_$n = \tau_n/\tau_p$, ratio_$m = \tau_f/\tau_p$. The physical parameters of NdFeB and ferrite grades are shown in Table 2.

4.2 | Analysis results

In this section, the ratio of NdFeB and ferrite magnets is analysed to make the mean force close to that of the all rare-earth model, while reducing the force ripple and THD.

Because the optimal ratio of magnet in the all-NdFeB mover is 0.6, in the absence of saturation, the larger the ratio of magnet, the larger the mean force, for the combination of ferrite and NdFeB; the ratio of NdFeB will not be in excess of 0.6. Compared with the NdFeB, the residual magnetism and the coercive force of the ferrite magnets are almost just 30% of the NdFeB, so in order not to affect the mean force of this PMSLM, only a comparatively smaller section of the NdFeB is replaced by the ferrite. Ratios of NdFeB magnet of 0.4 and 0.5 are selected as shown by the parameter 'ratio_*n*' in Table 3. When the ratio of NdFeB, 'ratio_*n*', is 0.5, it follows from the mathematical definition of 'ratio_*m*' that the maximum ratio of ferrite magnets is 0.25, as shown in Table 3.

4.3 | Design verification by simulation

Three models are established in this section, with the parameters of the primary remaining the same, while for the secondary, the PM material and usage are different, as shown in Table 4. Model 1 is the same with the all rare-earth model of Section 2. Model 2 is with the new hybrid PM structure of Section 4, which is required to have a same mean force as with model 1. Finally, model 3 is also presented (which is used to cf. with model 2, and to verify that the usage of ferrite will increase the mean force of PMSLM).

The proposed PM structure will affect the magnetic flux density of the air gap, which in theory will change the cogging force and the end effect detent force. It is needed to investigate the impact for the two types of force.

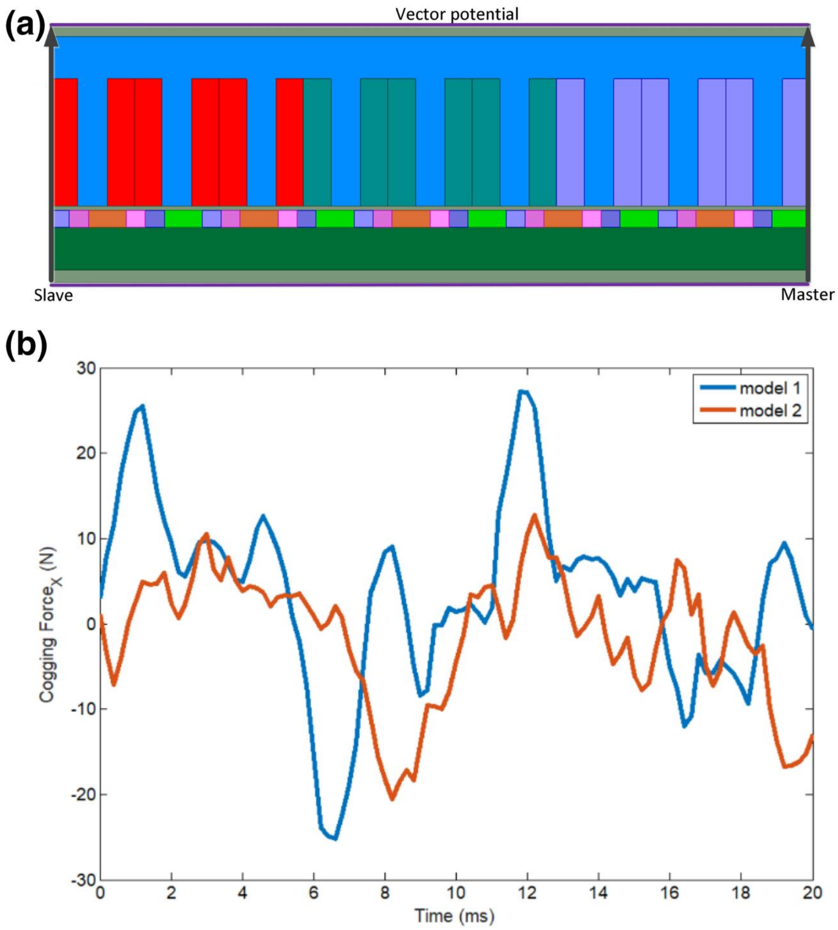

FIGURE 6 Cogging force simulation model and simulation calculation results. (a) Cogging force simulation model, (b) Cogging force curves of model 1 and model 2

4.4 | End effect force

In order to obtain the end-effect force of the PMSLM designs without considering the cogging force caused by slot and tooth effect, a simulation model, which is without the slot and tooth is established, is described in Figure 5(a).

Through the simulation, the end effect force of model 1 and model 2 is shown in Figure 5(b).

From Figure 5(b), it can be seen that there is an angle bias between the moving forces of the two models, but the peak value of force of model 2 is only 1.21 N that is lower that of model 1.

4.5 | Cogging force

In order to obtain the cogging force, a simulation model, which is loaded with periodic boundary condition, is established. In this case, the PMSLM can be considered as a PMSLM without end-effect, with the model described in Figure 6(a).

Through the simulation, the cogging force of model 1 and model 2 are obtained as in Figure 6(b).

From the Figure 6(b), it can be seen that the peak value of cogging force of model 2 is reduced by about 19.1N compared with that of model 1.

4.6 | Air-gap magnetic field distribution

The magnetic flux distributions in air gap for model 1 and model 2 are shown in Figure 7. From Figure 7, it can be seen that the main flux distribution for model 1 and model 2 are the same, which guarantees that the thrust force of model 1and model 2 is nearly the same as well. The slight difference can be located to the area between two adjacent NdFeB PMs, which are marked in Figure 7, and this phenomenon is attributed to the application of ferrite PMs. There is more linkage flux between two different polarities PMs, which affects the flux density in the air gap to change the cogging force and force density.

With the hybrid usage of NdFeB and ferrite, the magnetic flux density curves in the air gap of model 2 are different from that of model 1, which are shown in Figure 8(a), and the Fourier analysis results of the magnetic flux density distribution in the air gap are shown in Figure 8(b). As shown

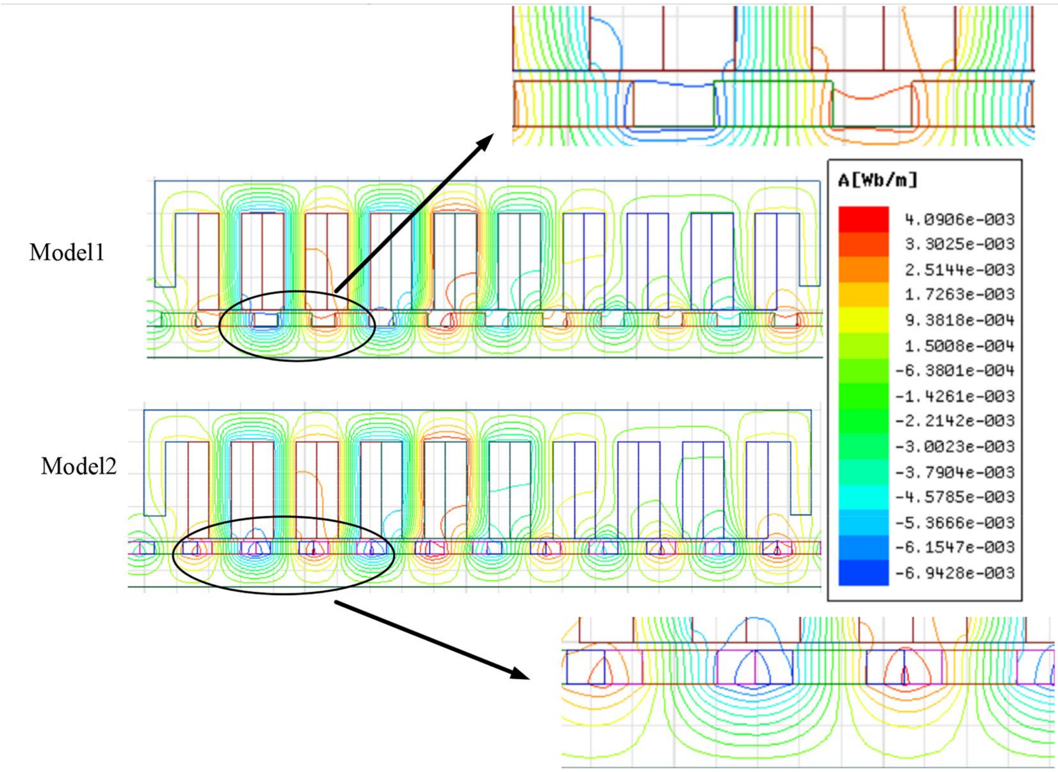

FIGURE 7 Flux distribution for model 1 and model 2

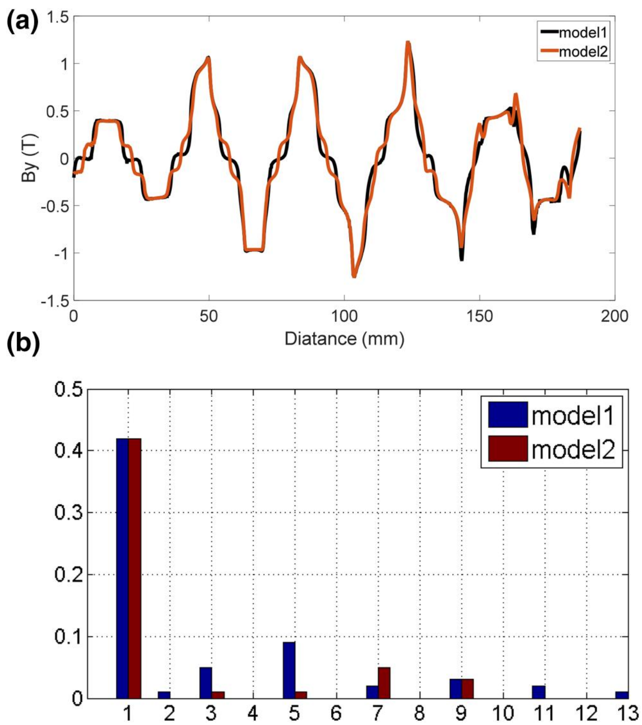

FIGURE 8 Air gap flux density curves and their Fourier decomposition for model 1 and model 2. (a) Air gap flux density curves for model 1 and model 2 and (b) Fourier analysis results for the air gap flux density of model 1 and model 2

in Figure 8(a), the sinusoidal quality of air gap flux density curves in model 1 and model 2 are different, and through the Fourier decomposition, shown in Figure 8(b), it can be seen that the third and fifth orders harmonic are reduced heavily for model 2 compared with model 1. The value of third order harmonic of model 2 is only the 20% of that of the model 1, and the value of fifth order harmonic of model 2 is only the 11.1% of that of the model 1.

4.7 | Back EMF analysis

The induced voltage is another important comparative factor for the performance of the PMSLM. The phase induced voltage of the three models is shown in Figure 9(a), and their Fourier analysis results are shown in Figure 9(b). As shown in Figure 9(a), the back electromotive force (EMF) curves for model 1 and model 2 are almost same, while for the model 3, the peak to peak value is a little lower than that of model 1 and model 2.

From Figure 9(b), it can be observed that the third order harmonics of model 2 is only half of that of model 1.

4.8 | Force analysis

The cogging force and force curves of model 1 and model 2 are shown in Figure 10, and the results are also summarized in Table 5.

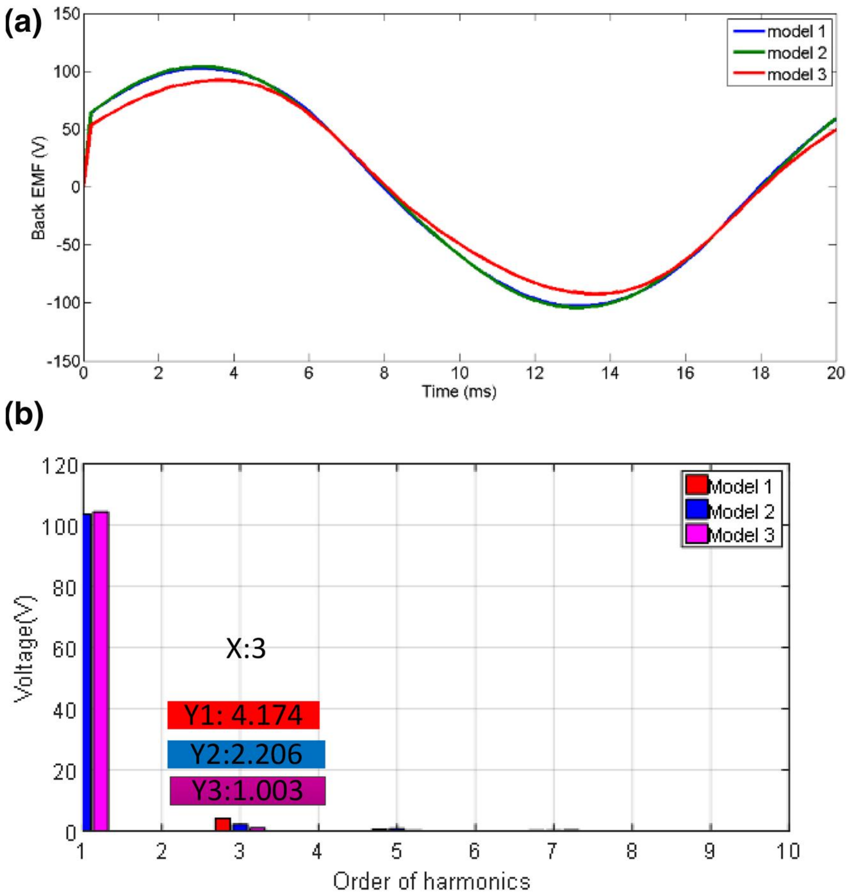

FIGURE 9 The induced voltage and their Fourier analysis results of the three models. (a) One phrase induced voltage and (b) Fourier analysis of induced voltage

For model 1, the mean force is 312.7 N, and the force ripple is 3.33%. For model 2, the mean force corresponding to the same current density is 315 N, which is at a same level as the original model, but the force ripple is reduced down to 2.47%. The mean force for model three is only 275 N, and the force ripple is 3.23%.

It can be seen that the hybrid usage of NdFeB and ferrite can reduce the force ripple. In this study, with this said method, the force ripple is reduced by almost 1%, from 3.33% down to 2.47% when comparing model 1 with model 2. Moreover, the reduction of the usage of NdFeB does not reduce the mean force for the same current loading. Comparing model 2 and model 3, with the same usage amount of NdFeB, the little usage of ferrite in model 2 can increase the mean force by about 40 N.

Besides, because the price of ferrite is less than 10% that of the NdFeB, although the total amount of PM materials is increased, the cost of PM reduces by around 25%. In arriving at this conclusion, $/kg numbers for NdFeB and ferrite magnets are used, as shown in Table 6. From this table, it can be seen that the PM price of model 2 is reduced nearly 24% compared with that of model 1.

5 | EXPERIMENTAL VERIFICATION OF MODELLING TECHNIQUES

To give confidence to the analysis techniques, the results presented for the all-rare-earth mover (model 1) PMSLM and hybrid-magnet mover (model 2) are prototyped and the measurement platform is built, as shown in Figure 11. The platform consists of the 9-slot 10-pole PMSLM (one with all-rare-earth mover and another with hybrid-magnet mover, and the two protypes take turns to be tested), a ball-screw platform acting as the load of the PMSLM, an actuator, a controller, a DC power source, a tension sensor, an oscilloscope, a power analyzer WT1800, and a multichannel temperature tester GP10. The tension sensors are the connected bridge for this PMSLM and the ballscrew platform. The actuator is used to drive the PMSLM, and the controller is used to control the ballscrew, which is powered by the DC power source. The force curves are recorded using the oscilloscope, and the input power source is tested by the power analyser.

In the experiment, it is assured that the PMSLMs and the ballscrew platform are at the same level, and that the linear motor does the reciprocating motion to compress the tension sensor in order to obtain the forces and the cogging force.

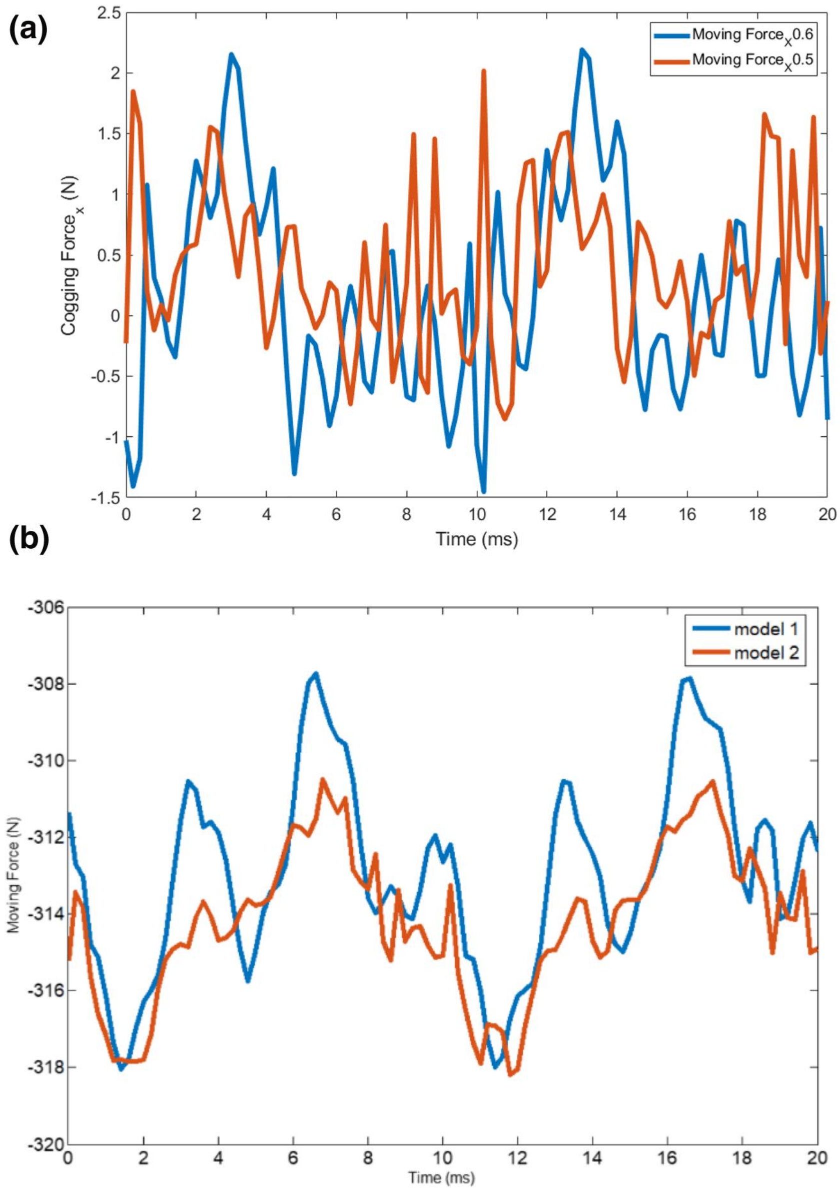

FIGURE 10 Cogging force and force curves of model 1 and model 2. (a) Cogging force for model 1 and model 2 and (b) Force for three models

TABLE 5 Force comparison for three models

Model	Mean force	Force ripple
Model 1	312.7 N	3.33%
Model 2	315 N	2.47%
Model 3	275 N	3.23%

In order to avoid the excessive sampling pulse, burr and noise of the oscilloscope, the opposite and positive force are separated from the curve, and the cogging force curves of the two PMSLMs are shown in Figure 12. The peak-to-peak value of cogging force for the original protypes (with all rare-earth PMs) is about 4.7 N, which is slightly higher than the simulated value, with the difference which can be mainly rooted to the manufacturing imperfections. Importantly, the peak-to-peak value of cogging force is lower.

The measured moving force of the two protypes is shown in Figure 13. From Figure 13, it can be seen that the protype with hybrid PMs has the same level force value with that of the PMSLM with all rare-earth PMs, which further verify the proposed structure of mover.

6 | CONCLUSION

The paper has compared in detail PMSLM with movers featuring all-rare-earth and hybrid magnet configurations. The structure analysis and simulation are adopted to analyse the performance of these two topologies of PMSLM. The hybrid-magnet structure has the merit of reducing the cogging force, together with the low-order flux density harmonics in the air gap. Furthermore, the third harmonic of the back EMF is reduced heavily. The mean force ripple for the 9-slot 10-pole

TABLE 6 Cost comparison for three models

Model	Mass of NdFeB of a Pole pitch*10^{-3} (kg)	Mass of ferrite of a Pole pitch*10^{-3} (kg)	Cost of PM/kg ($)
Model 1	37.8	0	5.67
Model 2	27	17.64	4.31
Model 3	27	0	4.05

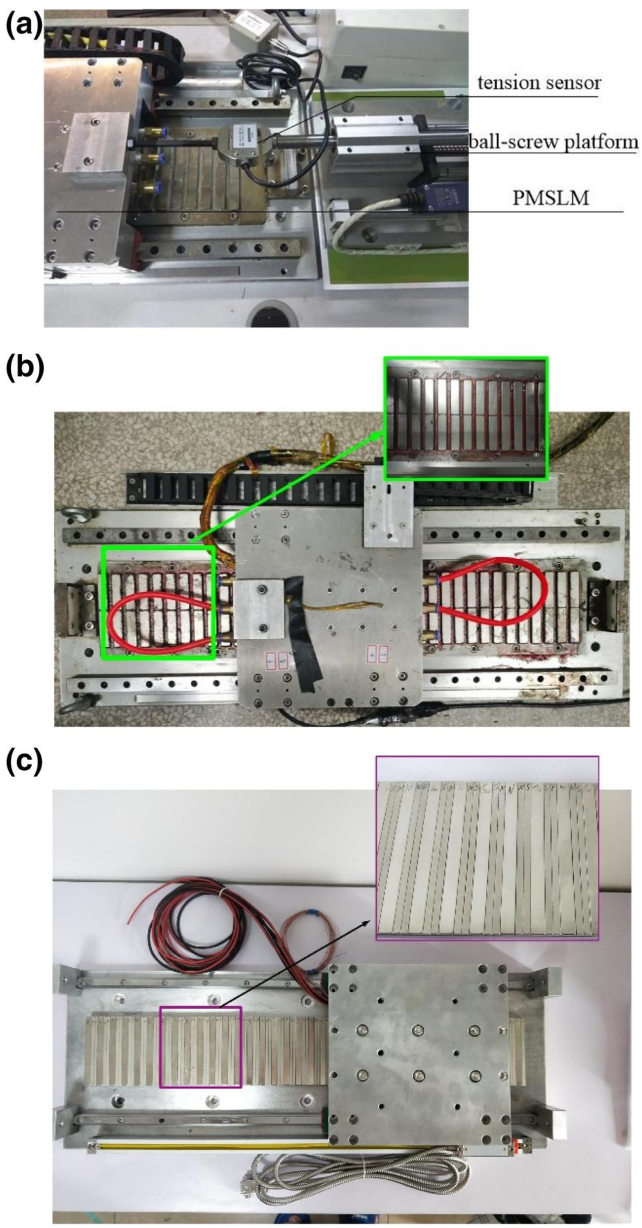

FIGURE 11 Experiment platform and protypes (a) experiment platform (b) all rare-earth (c) hybrid magnet

PMSLM can be reduced by 25.8%, from 3.33% to 2.47%, while the permanent magnet material cost can be reduced about 25%. In the end, the correctness of the modelling in this paper is verified by the experimental tests, putting confidence in the techniques used and results presented.

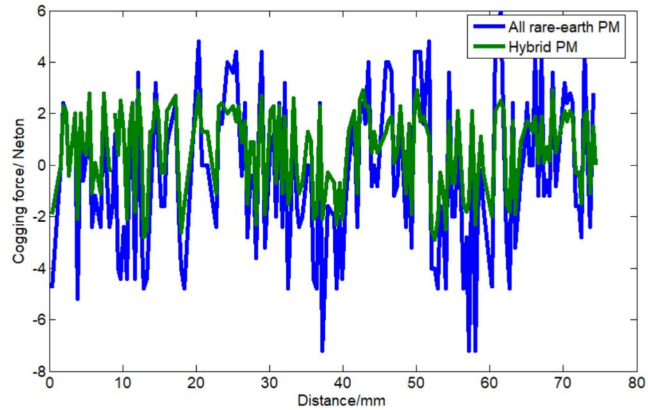

FIGURE 12 Cogging force measurement and analysis results for two protypes

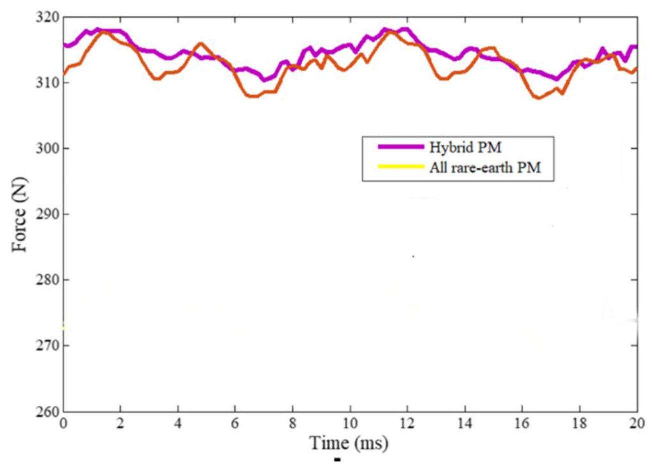

FIGURE 13 Force measurement and analysis results for two protypes

ORCID

Xiaomei Liu https://orcid.org/0000-0002-7011-4009
David Gerada https://orcid.org/0000-0002-8280-1308

REFERENCES

1. Kwon, Y.S., Kim, W.J.: Electromagnetic analysis and steady-state performance of double-Sided flat linear motor using soft magnetic composite. IEEE Trans Ind Electron. 64(3), 2178–2187 (2017)
2. Ma, Q., El-Refaie, A., Lequesne, B.: Low-cost interior permanent magnet machine with multiple magnet types. IEEE Trans Ind Appl. https://doi.org/10.1109/TIA.2020.2966458
3. Tan, Y.T., Shen, J.X.: Optimal design and vector control of an interior ferrite permanent magnet synchronous motor. In: 2017 20th

International Conference on Electrical Machines and Systems(ICEMS), pp. 1–6. (2017)
4. Huang, X., et al.: Detent force, thrust, and normal force of the short-primary double-sided permanent magnet linear synchronous motor with slot-shift structure. IEEE Trans Energy Convers. 34(3), 1411–1421 (2019)
5. Shokri, M., et al.: Comparison of performance characteristics of axial-flux permanent-magnet synchronous machine with different magnet shapes. IEEE Trans Magn. 51(12), 1–6 (2015)
6. Chai, F., et al.: Magnet shape optimization of surface-mounted permanent-magnet motors to reduce harmonic iron losses. IEEE Trans Magn. 52(7), 1–4 (2016)
7. Liang, P., et al.: Analytical prediction of magnetic field distribution in spoke-type permanent-magnet synchronous machines accounting for bridge saturation and magnet shape. IEEE Trans Ind. Electron. 64(5), 3479–3488 (2017)
8. Raza, M., et al.: Performance comparison of dual airgap and single airgap spoke-type permanent-magnet vernier machines. IEEE Trans. Magn. 53(6), 1–4 (2017)
9. Morimoto, S., et al.: Experimental evaluation of a rare-earth-free PMASynRM with ferrite magnets for automotive applications. IEEE Trans Ind Electron. 61(10), 5749–5756 (2014)
10. Kim, H.J., Kim, D.Y., Hong, J.P.: Structure of concentrated-flux-type interior permanent-magnet synchronous motors using ferrite permanent magnets. IEEE Trans Magn. 50(11), 1–4 (2014)
11. Tootoonchian, F., Nasiri-Gheidari, Z.: Cogging force mitigation techniques in a modular linear permanent magnet motor. IET Electr. Power Appl. 10(7), 667–674 (2015)
12. Vaez-Zadeh, S., Isfahani, A.H.: Multiobjective design optimization of air-core linear permanent-magnet synchronous motors for improved thrust and low magnet consumption. IEEE Trans. Magn. 42(3), 446–452 (2006)
13. Tavana, N.R., Shoulaie, A.: Minimizing thrust fluctuation in linear permanent-magnet synchronous motor with Halbach array. In: 2010 1st power Electronic drive Systems Technologies Conference (PEDSTC), pp. 302–306. (2010)
14. Wang, K., Zhu, Z.Q., Ombach, G.: Torque improvement of five-phase surface-mounted permanent magnet machine using third-order harmonic. In: 2016 IEEE Power and Energy Society General meeting, pp. 1–1. PESGM (2016)
15. Isfahani, A.H., Vaez-Zadeh, S., Rahman, M.A.: Using modular Poles for shape optimization of flux density distribution in permanent-magnet machines. IEEE Trans. Magn. 44(8), 2009–2015 (2008)

How to cite this article: Liu X, Yu H, Gerada D, et al. Comparison of rare-earth and hybrid-magnet mover configurations for a permanent magnet synchronous linear motor. *IET Electr. Power Appl.* 2021;15:321–331. https://doi.org/10.1049/elp2.12024

APPENDICES

τ_s Slot pitch, mm
τ_p Pole pitch, mm
g Width of airgap, mm
d_i Current density, A/mm^2
s Slot filling factor
h_m Height of PM, mm
height of the PMs, mm
h_w Width of PM, mm
h_m Height of PM, mm
height of the PMs, mm
τ_n width of NdFeB, mm
τ_f width of ferrite, mm
R_F Force ripple
F_{mean} Mean force, N
$F_{cogging}$ Cogging force, N
E_P Electromagnetic power, W
x moving distance of the primary, mm
F thrust force, N
W co-energy in the air gap, W
i current, A
μ_0 magnetic permeability of air,
B magnetic flux density, T
$\underrightarrow{V}$ volume of the air-gap and PM areas, mm^3
M magnetization vector of a PMLM with two different PM materials
M_x component of M in x direction, AT
M_y component of M in y direction, AT
B_r remanence of PMs, T
B_x tangential flux density of the component, T
B_y normal flux density of the component. T
F_R right lateral force of the iron, N
F_L left lateral force of the iron, N
$B_{0x1}(y)$ normal flux density of the left end-face, T
$B_{0x2}(y)$ normal flux density of the right end-face, T
L_a width of the primary iron, mm
G relative permeance
B_{0y} end-flux density of the PMSLM, T
B_{2n-1} amplitude of harmonic component, T
Δ displacement of the mover, mm
b half-length of the primary iron, mm
w_f distance between two adjacent secondary magnets, mm
B_1 amplitude of the fundamental component, T